A Design Methodology of Multi-Resonant Controllers for High Performance 400Hz Ground Power Units

Felix Rojas, *IEEE Member,* Roberto Cardenas, *IEEE Senior Member,* Jon Clare, *IEEE Senior Member,* Matias Diaz, *IEEE Member,* Javier Pereda, *IEEE Member,* and Ralph Kennel, *IEEE Senior Member.*

***Abstract*—In aerospace applications, a Ground Power Unit (GPU) has to provide balanced and sinusoidal $400\ Hz$ phase-to-neutral voltages to unbalanced and non-linear single-phase loads. Compensation of high-order harmonics is complex, as the ratio between sampling frequency and compensated harmonics can be very small. Thus multiple superimposed resonant controllers or PI nested controllers in multiple dq frames are not good alternatives. The first approach cannot ensure stability, while the second cannot track sinusoidal zero-sequence components, typically present in unbalanced system, and unachievable high bandwidth at the inner current control loop is typically required. In this paper, a simple methodology for designing a single-loop, multiple resonant controller for simultaneous mitigation of several high-order harmonics, ensuring stability, is presented. Experimental results, based on a 6kW four-leg NPC converter, validates the proposed controller design, showing excellent steady state and transient performance.**

***Index Terms*—Four-Leg Converters, Three level Neutral Point Clamped (NPC) inverter, Resonant Controllers.**

I. Introduction

Recently the aircraft industry has faced a tremendous development in the technology used for communication, services and control systems within an aircraft [1]. Electronic devices have played a fundamental role in this growth, leading to a more complex and sophisticated electrical system within the plane, which has to fulfill stringent power quality and safety regulations [2], [3]. When the aircraft is on ground, a power converter based Ground Power Unit (GPU) is connected to it, providing 110V phase-to-neutral at 400 Hz [2].

The authors acknowledge the support of the Chilean Research Council CONICYT under grant Fondecyt 1171142, Grant FONDAP 15110019 SERC Chile and Grant Basal Project FB0008 AC3E. Félix Rojas and Matías Díaz are with the Electrical Engineering Department, University of Santiago of Chile, Avenida Ecuador Nº 3519, Estacion Central, Santiago (e-mail: felix.rojas@usach.cl; matias.diazd@usach.cl). Roberto Cárdenas is with the Electrical Engineering Department, University of Chile, Avenida Tupper 2007, Santiago, Chile (e-mail: rcd@ieee.org). Jon Clare is with the Department of Electrical and Electronic Engineering, University of Nottingham, Nottingham University Park, Nottingham, NG7, 2RD, (e-mail: jon.clare@nottingham.ac.uk). Javier Pereda is with the Department of Electrical Engineering and the UC Energy Research Center, Pontificia Universidad Católica de Chile, Santiago 7820436, Chile (e-mail: jepereda@ing.puc.cl). Ralph Kennel is with the Institute for Electrical Drive Systems and Power Electronics, Technical University of Munich, Arcisstr. 21, 80333, Munich (email: ralph.kennel@tum.de).

The aircraft electrical system is four-wire unbalanced system, with many individual loads connected phase-to-neutral. Therefore, a GPU is a four-wire power supply rated at 110V (phase), 400Hz and typically between 30-180kVA (being 90kVA the most utilized power rate) [4].

Different solutions have been proposed for power electronics based GPUs [5]. Typically, three H-bridges connected in parallel, sharing the same dc-link and connected to LC filters, are used to independently control each phase-to-neutral voltage. However, the compensation of high order harmonic components is limited by the switching frequency. An alternative configuration uses transformers to add the output voltages of several inverters, generating a stepped waveform [6]. Although this configuration offers good THD with low switching frequency, it is complex to control and the high number of elements reduces its reliability. Recently new topologies such as matrix converters have been proposed for GPU applications [7], [8]. Despite advantages in terms of size and weight, this approach has a high number of switches and for unbalanced load operation produces distorted currents with low power quality in the input side of the converter.

The relatively high output frequency of the GPU is an issue for design. Standard 50/60 Hz Uninterruptible Power Supply (UPS) converters typically have sampling frequencies between 2-12kHz. The high ratio between the fundamental and the sampling frequency allows many control schemes, such as: nested *d-q* controllers, resonant controllers, repetitive and predictive controllers [9]–[11] to be implemented relatively easily. However, for a 400 Hz GPU, a 2 kHz sampling frequency is not feasible, because the ratio between the fundamental and the sampling frequency is insufficient. Therefore, for a GPU, the sampling frequency typically has to be around 10-15 kHz and even higher when harmonic compensation is required. Moreover, the high bandwidth required for an inner current control loop means the use of double-loop structures for nested voltage/current controllers is not practically implementable and the use of single-loop voltage controllers have been preferred for this application. In [4] a robust single-loop strategy has been proposed to control the output voltage of a GPU and whilst it achieves good performance with linear loads, it is not capable of compensating harmonic distortion with non-linear loads.

Due to their simple and robust implementation, resonant controllers are an interesting solution for high order harmonic

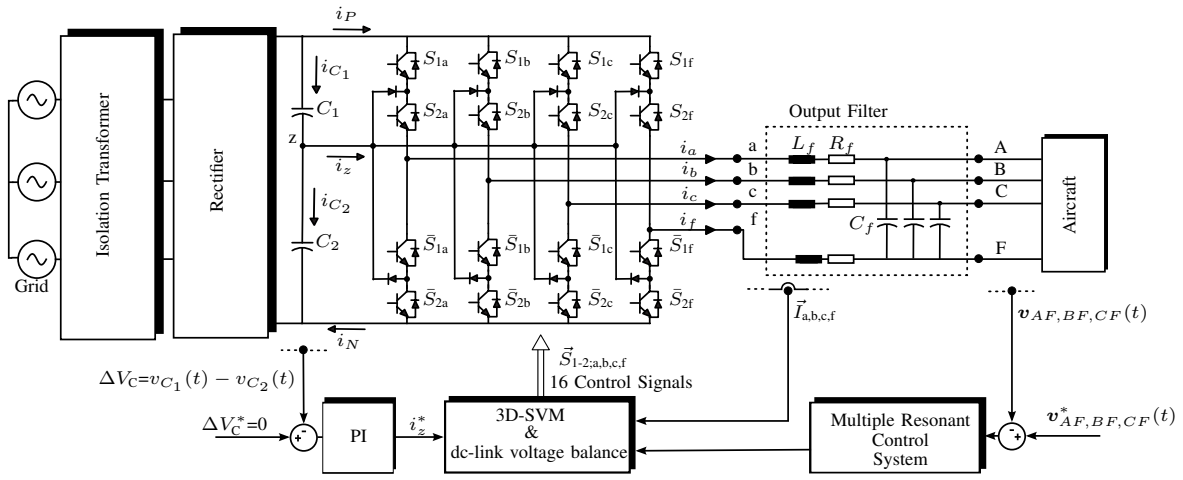

Fig. 1. Control scheme for the proposed four-leg NPC converter used as GPU. An small output LC filter is used to obtain 400Hz sinusoidal output voltages. R_f represents the series resistance, L_f is the filter inductance and C_f is the capacitor of the filter.

compensation. They have been used for selective harmonic elimination in several applications [5], [7], [12]. However, careful consideration of stability margins and the selection of discretization method are important during the controller design to ensure stability, particularly when high order harmonics have to be compensated [13]–[15]. In [5] a resonant controller has been proposed as a solution for a standard two-level, 400 Hz GPU. The implementation includes third, fifth and seventh order harmonic compensation but cannot be reasonably extended to higher order harmonics such as 11^{th} $(4.4kHz)$, 13^{th} $(5.2kHz)$ or 15^{th} $(6kHz)$ as the power losses of the converter limit the switching frequency and therefore the higher order harmonic compensation. Furthermore, no stability analysis has been undertaken in [5].

The contributions of this paper can be summarized as follows:

- A simple methodology for designing a single-loop resonant controller with multiple resonances, for regulation of the fundamental 400 Hz voltage signal as well as compensation of high order harmonics components, under non-linear and unbalanced loads, is proposed and successfully validated. The methodology allows direct design of one controller with multiple resonances, avoiding the superposition of individually designed resonant controllers as presented in [16], [17]. Multiple dq frame transformations and positive-negative sequence decomposition are avoided, which is an important advantage over other published methods [18], [19].
- The proposed methodology can be used to design a robust and more stable control system when the sampling frequency is close the Shannon-Nyquist frequency (theoretical limitation). This is important for a 400Hz GPU application. An analytical design for the full discretized controller based on Nyquist response, considering delay compensation is proposed in this paper and experimentally validated. This improves stability and robustness, when a non-damped resonant LC output filter is implemented and the sampling frequency is close to the compensated harmonic components.
- A four-leg three-level Neutral Point Clamped (NPC) has been validated as a suitable solution for a $400Hz$ GPU application. The multi-level nature of this topology increases the equivalent frequency of the modulated waveform compared to the switching frequency of each device, which is a major advantage for the GPU, allowing higher-order harmonic compensation compared to the two-level VSI typically reported in the literature [5], [13], [16]–[18]. The fourth leg of the converter provides a path for zero-sequence current components, i.e. unbalanced loads, producing 5-levels phase-to-neutral output voltages which allows implementation of smaller output power filters with lower reactive power consumption [20].

The rest of this paper is organized as follows. In Section II the proposed control methodology is introduced and extensively analyzed. Three-dimensional modulation is discussed in Section III. Experimental results are discussed in section IV.

II. Single-loop Voltage Control Strategy

Resonant controllers and rotating *dq* controllers are the most suitable alternatives for single-loop voltage control of grid connected and stand alone power converters [13], [21]–[23]. Both schemes provide good transient and steady-state performance. However, when unbalanced and harmonic compensation are required, resonant controllers are simpler to design and require less computational burden. They avoid multiple reference frames transformations and positive/negative sequence separation and give direct control over the zero-sequence present in four-wire systems.

Fig. 1 shows the proposed solution for a 400Hz, 110V GPU, where the aircraft represents a linear/non-linear, balanced/unbalanced load. A small *LC* filter is used at the output of the converter. A single-loop resonant controller controls the output voltage of the GPU, compensating third, fifth, seventh, ninth and eleventh harmonics. A three-dimensional SVM algorithm in $\alpha\beta\gamma$ coordinates is used to synthesize the output voltages [24]. Furthermore, using the redundant

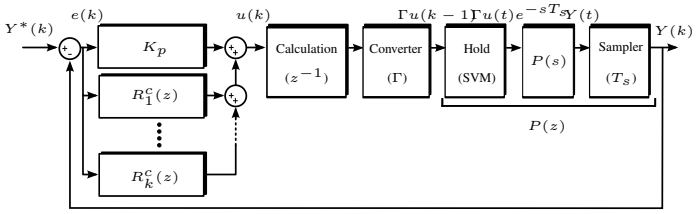

Fig. 2. Discrete-time single-loop control structure for implementation of resonant controllers. $Y^*(k)$ and $Y(k)$ represents the reference and controlled discrete-time variables. $R_n^c(z)$ for $n = \{1, 2, .., k\}$ represent a resonant controller with delay compensation for compensation of a signal with frequency ω_n in discrete-time.

vectors of the four-leg NPC and output current measurements, a PI controller is used to balance the voltage on the dc-link capacitors.

The transfer function of the second-order *LC* filter shown in Fig. 1 is:

$$P(s) = \frac{V_o(s)}{V_i(s)} = \frac{1}{L_f C_f s^2 + R_f C_f s + 1} \tag{1}$$

where L_f, R_f and C_f represents the parameters of the *LC* filter.

The resonant controller design must provide sufficient stability margins for each of the compensated harmonics. Hence, the controller is implemented with angle compensation with a transfer function given by:

$$G^c(s) = \sum_{n=1}^{k} R_n^c(s) = \sum_{n=1}^{k} K_n \frac{s\cos\vartheta_n - \omega_n \sin\vartheta_n}{s^2 + \omega_n^2} \tag{2}$$

where K_n represents the gain and ω_n is the resonance frequency for the n^{th} resonant compensator. Furthermore, the phase of each compensator can be modified by adjusting ϑ_n. Setting this angle as: $\vartheta_n = -\angle P_d(j\omega_n)$, compensates the phase shift injected by the plant, giving an open-loop phase shift of $\pm 90^\circ$ around the resonance frequencies and increasing the stability margin of the closed-loop system.

Notice that ϑ_n compensates both the phase shift introduced by the plant (at the resonant frequencies ω_n) and also the loss of phase margin produced by the one sample time delay introduced by the SVM algorithm.

A. Discrete Time Representation

To implement the controller in a digital platform, a discrete time representation and design for the controller and the plant are required. Fig. 2 presents the discrete-time control scheme of a resonant controller implemented for a second order system. The control algorithm calculation time is represented as a unit delay and the VSI is represented as a constant gain.

For the SVM algorithm, the output voltages of the *LC* filter are measured every sampling time T_s. Furthermore, the output voltages of the converter are maintained constant during each sampling time T_s. Therefore, the plant can be considered as a continuous system cascaded with a Zero-Order Hold (ZOH) circuit and a sampled output. Thereby, the ZOH discrete representation (see [15]) of the second order system of (1) is given by:

$$P^{zoh}(z) = 1 - \frac{z-1}{\sqrt{1-\xi^2}} \left(\frac{z e^{-\xi\omega_{nat}T_s}\sqrt{1-\xi^2}\sin\left(T_s\omega_{nat}\sqrt{1-\xi^2} - arcos(\xi)\right)}{z^2 - 2ze^{-\xi\omega_{nat}T_s}\cos\left(T_s\omega_{nat}\sqrt{1-\xi^2}\right) + e^{-2\xi\omega_{nat}T_s}} \right) \tag{3}$$

$$\omega_{nat} = \frac{1}{\sqrt{L_f C_f}} \tag{4}$$

$$\xi = \frac{R_f\sqrt{L_f C_f}}{2L_f} \tag{5}$$

To ensure zero steady state error to sinusoidal reference signals, the discretization method applied to (2) must maintain the resonant frequencies ω_n unaltered, providing infinite gain at each of these frequencies [13], [14]. Accordingly, the First Order Hold (FOH) and Tustin with Prewarping (TPW) methods, setting the prewarping frequency as each ω_n, are suitable approximations of the continuous system. Thus, using the FOH approximation, the discrete form of the resonant controller of (2) is given by:

$$R^{c-foh}(z) = \sum_{n=1}^{k} K_n \frac{cos(\omega_n D_n T_s)(1-z^{-2})(1-cos(\omega_n T_s)))}{\omega_n^2 T_s(1-2z^{-1}cos(\omega_n T_s)+z^{-2})} - \tag{6}$$

$$\frac{sin(\omega_n D_n T_s)\left[\omega_n T_s - sin(\omega_n T_s) + 2z^{-1}sin(\omega_n T_s)\right]}{\omega_n^2 T_s(1-2z^{-1}cos(\omega_n T_s)+z^{-2})} -$$

$$\frac{sin(\omega_n D_n T_s)\left[-2z^{-1}\omega_n T_s cos(\omega_n T_s) + z^{-2}(\omega_n T_s - sin(\omega_n T_s))\right]}{\omega_n^2 T_s(1-2z^{-1}cos(\omega_n T_s)+z^{-2})}$$

where T_s is the sampling time used for the discretization and ω_n is the resonance frequency of the n^{th} resonant controller. The term D_n represents the number of samples required for compensating the phase-shift introduced by the plant. Equivalently to ϑ_n of (2), D_n for the n^{th} resonant controller is given by:

$$D_n = \frac{-\angle P^{zoh}(z_n = e^{j\omega_n T_s})rad}{T_s\omega_n} \tag{7}$$

where $P^{zoh}(z_n = e^{j\omega_n T_s})$ represents the ZOH discrete-time representation of (3) evaluated at the resonance frequency ω_n.

B. Controller Design

Different strategies has been proposed in the literature for the design of resonant controllers employing Nyquist diagrams [13], [16]–[19]. However, those approaches usually use a first order plant or make a first order approximation, neglecting the resonant effect of a higher order filter. This allows independent design for each resonant compensator, which can be useful when the resonance of the filter is far from the resonance of each compensator. However, when high order harmonics relatively close to the resonance of the filter have to be compensated, an independent design of each compensator can lead to instability. Therefore, a design considering all the resonant compensators in a single transfer function is required and studied in this section.

Fig. 3 shows the Bode and Nyquist response for the open loop system $H_1(s) = G(s)P(s)e^{-sT_s}$, considering the

resonant controller of (2), tuned only at the fundamental 400Hz frequency with $\vartheta_1 = 0°$, and the second order filter of (1). Fig. 3a shows the bode plot of $H_1(s)$ for three different gains $K_{1a,1b,1c}$ including a sampling time delay T_s. The later introduces a phase shift of $-10°$ at ω_1, and the phase of $H_1(s)$ steps from $\xi_1 = 80°$ to $\xi_1 - 180°$ at ω_1. Fig. 3b shows the Nyquist diagram of $H_1(s)$ for the three different gains $K_{1a,1b,1c}$. The Nyquist diagram starts from the point $(0, 0j)$ at $\omega = 0\ rads^{-1}$, as ω approaches from 0 to ω_1, the magnitude of $H_1(s)$ increases towards infinity with an angle ξ_1. After $\omega > \omega_1$, the phase of the Nyquist plot turns rapidly through $180°$ to appear from the bottom of the frame. Thereafter, instead of approaching directly to zero, the Nyquist plot describes a curve which approaches towards the left side of the plane, making possible to enclose the critical stability point $(-1, 0j)$. This curve is produced by the resonance of the second order filter ω_c, defining the stability margin of the closed-loop system and representing a constraint for the gain of the controller in order to maintain closed-loop stability. From Fig. 3b, the curve κ_c leads to an unstable system, nevertheless the phase margin of the open loop system, before the resonance peak is $\approx 90°$. This shows one of the problems of Bode diagrams to design resonant control systems, especially when multiple resonant controllers are implemented. There are many frequencies where the magnitude of $G(s)H(s)$ crosses the 0db line (e.g see Fig. 5). Therefore it is difficult to predict the performance and overall stability using a Bode diagram and phase margins, in control systems where multiple resonant controllers are implemented. For this reason Nyquist diagrams are preferred in this work, because they have significant advantages for the design of high-order controllers with multiple resonant peaks.

Additionally, from Fig. 3b it is concluded that for an angle $\xi_1 < 0$ the Nyquist path would enclose the point $(-1, 0j)$ regardless of the controller gain. This is of particular importance when high order harmonics have to be compensated, as the phase of the open loop system rapidly decreases as a result of the phase injected by the sampling delay $P_d(s) = P(s)e^{-sT_s}$. Thereby, to increase the stability margin of the closed-loop system it is desirable to set ξ_1 to $90°$ at the resonance frequency ω_1. Thereby, to set each angle ξ_n to $90°$, the phase shift produced by the plant at each resonance frequency, $\vartheta_n = -\angle P_d(j\omega_n)$, has to be compensated in (2).

Fig. 4a shows the open-loop bode diagram of $H_1^c(s) = P_d(s)G_1^c(s)$ considering a resonant controller to regulate the 400Hz fundamental including the phase compensation. The phase shift is now $\pm 90°$ at the resonance frequency ω_1. Similarly to Fig. 3b, Fig. 4b shows the Nyquist diagram for the open-loop system considering phase compensation ($H_1^c(s)$). The introduction of the phase shift compensation allows placement of the asymptotes parallel to the $j\omega$ axis ($\xi_1 = 90°$), which helps to maintain the stability of the closed-loop system when high frequencies are compensated. The paths σ_1 and σ_2 show the trajectory of the Nyquist response as ω approaches the resonance frequency ω_1. Additionally the magnitude of the closed-loop frequency response, i.e. M circle tangent to the Nyquist response, has been plotted in order to set the gain of the controller K_1 for obtaining a damping factor

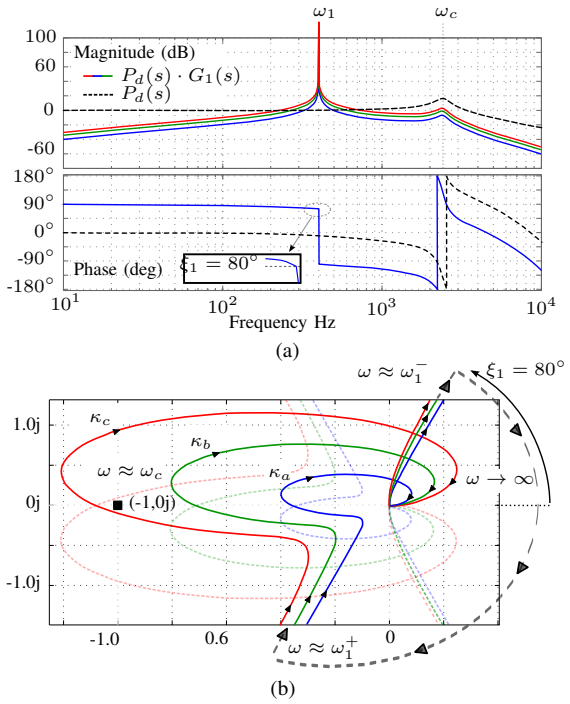

Fig. 3. (a) Bode and (b) Nyquist diagram for the open-loop system $H_1(s) = G_1(s)P_d(s)$. $P_d(s) = P(s) \cdot e^{-sT_s}$, $T_s = 1/16800$ s, $P(s)$ with $R_f = 0.5\ \Omega$, $L_f = 219\ \mu$H and $C_f = 20\ \mu$F posses a resonance at $\omega_c \approx 2\pi \cdot 2400$ rad/s. $G_1(s) = K_1 \frac{s}{s^2+\omega_1^2}$, $\omega_1 = 2\pi \cdot 400$ rad/s and three different gains have been used $K_{1a} = 1000$, $K_{1b} = 2000$ and $K_{1c} = 3000$. In (b), $\kappa_{a,b,c}$ represent Nyquist plot for the gains $K_{1a,1b,1c}$, the dotted semitransparent lines represents the Nyquist response for negative frequencies.

of $\zeta = 0.65$. The damping factor ζ and the magnitude of the closed-loop frequency response are related by [15]:

$$M \approx \frac{1}{2\zeta\sqrt{1-\zeta^2}} \tag{8}$$

Fig. 5 shows the Bode and Nyquist diagram for the open loop system composed of $P_d(s)$ and a resonant voltage controller to regulate not only the fundamental 400 Hz frequency, but to eliminate all the odd harmonics up to the eleventh. As expected, Fig. 5a possesses six resonant peaks at the frequencies $\omega_{1,3,5,7,9,11}$ with $\pm 90°$ phase shift around the resonance frequencies. The phase compensation places the asymptotes, for each resonance frequency $\omega_{1,3,5,7,9,11}$, parallel to the $j\omega$ axis in the Nyquist diagram of Fig. 5b, which reduces the possibility of enclosing the critical point $(-1, 0j)$. Equivalent to Fig. 4b, from Fig. 5b a set of paths σ_1 to σ_{12} can be recognized. The frequency increases starting from 0 Hz along the trajectory described by σ_1, the magnitude of the Nyquist plot increases to infinity (with an angle of $90°$) at the resonant frequency ω_1, thereafter the plot moves to the bottom of the diagram with an angle of $-90°$ (trajectory σ_2). Similar trajectories are produced for each resonant frequency, thus: σ_3-σ_4 for ω_3, σ_5-σ_6 for ω_5, etc. Although the gain of each compensator of $G_{1,3,5,7,9,11}^c(s)$ contributes to driving the Nyquist plot towards the critical point $(-1, 0j)$, the gains K_5 and K_7 have to be well limited as their associated peaks are closer to ω_c. Table I summarizes the angles injected by the plant and the computational delay in order to compensate ϑ_n

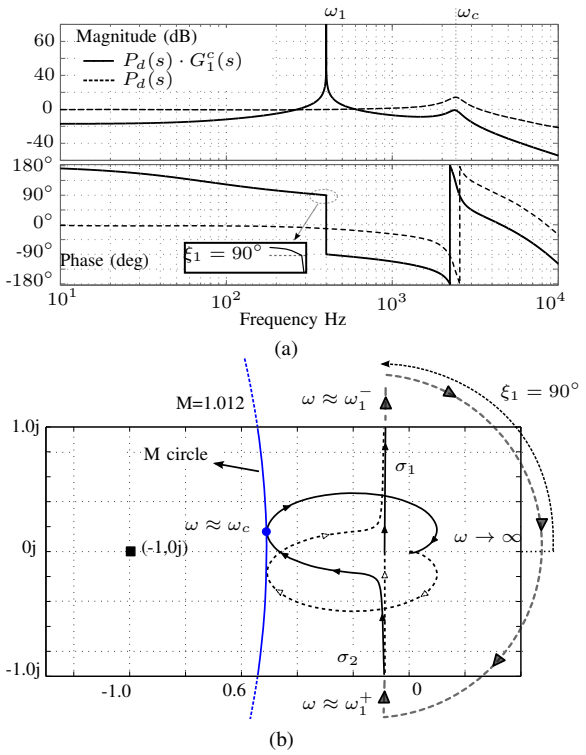

Fig. 4. (a) Bode and (b) Nyquist diagram for the open-loop system $H_1^c(s) = G_1^c(s)P_d(s)$. $P_d(s) = P(s) \cdot e^{-sT_s}$, $T_s = 1/16800$ s, $P(s)$ with $R_f = 0.5\Omega$, $L_f = 219$ μH and $C_f = 20$ μF posses a resonance at $\omega_c = 2\pi \cdot 2400$ rad/s. $G_1(s) = K_1 \frac{s\cos\vartheta_1 - \omega_1 \sin\vartheta_1}{s^2+\omega_1^2}$, $\omega_1 = 2\pi \cdot 400$ rad/s, $\vartheta_1 = -10°$, $K_1 = 1255$. In (b) Nyquist response for positive and negative frequencies (dotted lines) is shown. The tangent M circle for M=1.01, 2 is centred at (-42.41,0j) with a radius of 41.91 and associated with a damping factor of $\zeta = 0.65$.

TABLE I
ANGLE COMPENSATION ϑ_n FOR $G_{1,3,5,7,9,11}^c(s)$

R_n^c & σ_n	ω_n rad/s	-$\angle P(j\omega_n)$	-$\angle e^{-j\omega_n T_s}$	ϑ_n
$R_1^c(s)$ (σ_1, σ_2)	$2\pi \cdot 400$	1.48°	8.57°	10.05°
$R_3^c(s)$ (σ_3, σ_4)	$2\pi \cdot 1200$	5.73°	25.71°	31.44°
$R_5^c(s)$ (σ_5, σ_6)	$2\pi \cdot 2000$	22.17°	42.85°	65.03°
$R_7^c(s)$ (σ_7, σ_8)	$2\pi \cdot 2800$	153.68°	60°	213.68°
$R_9^c(s)$ (σ_9, σ_{10})	$2\pi \cdot 3600$	169.67°	77.14°	246.81°
$R_{11}^c(s)$ $(\sigma_{11}, \sigma_{12})$	$2\pi \cdot 4400$	173.28°	94.28°	267.56°

in each compensator. Additionally, the path σ_n of Fig. 5 related to each resonance frequency is also depicted.

III. THREE-DIMENSIONAL SPACE VECTOR MODULATION

To generate the voltage demanded by the multiple resonant controllers, the three-dimensional SVM presented in [24], [25] has been used. Fig. 6 shows the three-dimensional modulation space, where the reference vector can be modulated. This space is formed by 65 different vectors, where 14 vectors posses one redundancy and the zero vector possesses two redundancies, making up the $3^4 = 81$ switching states of the converter. For simplicity, only 14 vectors, that shape the modulation region, are represented in Fig. 6. The reference vector $\boldsymbol{v}^*_{\alpha\beta\gamma}$ is also depicted inside the modulation space. To obtain the modulation space of the converter, each of the 81 switching states are transformed using the Clarke transform

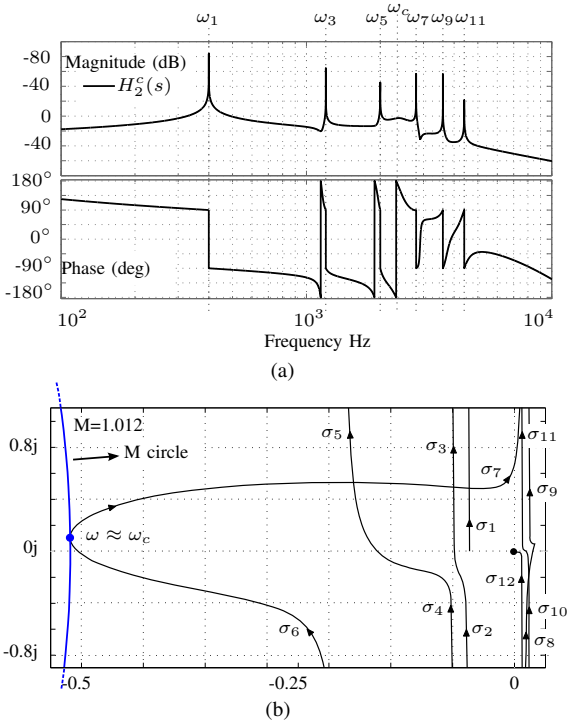

Fig. 5. (a) Bode and (b) Nyquist diagram for the open-loop system $H_2^c(s) = G_{1,3,5,7,9,11}^c(s)P_d(s)$. $P_d(s) = P(s) \cdot e^{-sT_s}$, $T_s = 1/16800$ s, $P(s)$ with $R_f = 0.5$ Ω, $L_f = 219$ μH and $C_f = 20$ μF posses a resonance at $\omega_c = 2\pi \cdot 2400$ rad/s. $G_{1,3,5,7,9,11}(s) = \sum_{n=1,3,5,7,9,11}^{1} K_n \frac{s\cos\vartheta_n - \omega_n \sin\vartheta_n}{s^2+\omega_n^2}$, $\omega_1 = 2\pi \cdot 400$ rad/s, $\omega_3 = 3\omega_1$ rad/s, $\omega_5 = 5\omega_1$ rad/s, $\omega_7 = 7\omega_1$ rad/s, $\omega_9 = 9\omega_1$ rad/s and $\omega_{11} = 11\omega_1$ rad/s. $K_1 = 610$, $K_{3,5,7,9,11} = 80$. In (b) Nyquist response for only positive frequencies is shown. The paths σ_1 to σ_n show the trajectory of the Nyquist response as $\omega \approx \omega_n^-$ and $\omega \approx \omega_n^+$ for each resonance frequency. The tangent M circle for M=1.012 is centred at (-42.41,0j) with a radius of 41.91 and associated to a damping factor of $\zeta = 0.65$.

(see Appendix) as presented in (9)-(11). The voltages used in (10) are referred to Fig. 1.

$$\boldsymbol{v}^i_{\alpha\beta\gamma} = \boldsymbol{T}^{\alpha\beta\gamma}_{abc} \boldsymbol{v}^i_{abc} \tag{9}$$

$$\boldsymbol{v}^i_{abc} = [v^i_{af}, v^i_{bf}, v^i_{cf}] \tag{10}$$

$$\boldsymbol{v}^*_{\alpha\beta\gamma} = \boldsymbol{T}^{\alpha\beta\gamma}_{abc} \boldsymbol{v}^*_{abc} \tag{11}$$

The reference vector $\boldsymbol{v}^*_{\alpha\beta\gamma}$, presented in Fig. 6, can be placed anywhere inside the modulation region and is generated by selecting the four nearest vectors at each sampling time. Thus, the first step to achieve modulation is to identify the four vectors that form the tetrahedron that enclose the reference vector. This can be achieved by the following simple steps:

$$\boldsymbol{v}_{0_{\alpha\beta\gamma}} = \boldsymbol{T}^{\alpha\beta\gamma}_{abc} \, \boldsymbol{floor}\,(\boldsymbol{v}^*_{abc}) \tag{12}$$

$$\boldsymbol{v}_{0'_{\alpha\beta\gamma}} = \boldsymbol{v}_{0_{\alpha\beta\gamma}} + [0,0,1] \tag{13}$$

$$\hat{\boldsymbol{v}}^*_{\alpha\beta\gamma} = \boldsymbol{v}^*_{\alpha\beta\gamma} - \boldsymbol{v}_{0_{\alpha\beta\gamma}} = [\hat{v}_\alpha, \hat{v}_\beta, \hat{v}_\gamma] \tag{14}$$

$$\phi = tan^{-1}\left(\frac{\hat{v}_\beta}{\hat{v}_\alpha}\right) \tag{15}$$

In (12) and (13) the first two vectors of the converter are selected, then, and similarly to the SVM algorithm for a two-level converter, based on the angle calculated on (15), the final two active vectors are selected, which are separated by 60° and

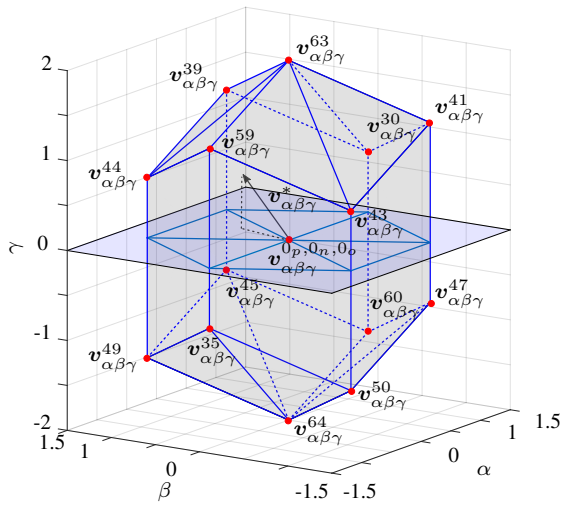

Fig. 6. Modulation Region for a three-level four-leg Neutral Point Clamped Converter.

have a constant amplitude. Thereafter, the duty cycles for each vector can be calculated as:

$$\begin{bmatrix} d_2 \\ d_3 \\ d_4 \end{bmatrix} = \boldsymbol{D_n} \begin{bmatrix} \hat{\boldsymbol{v}}^*_\alpha \\ \hat{\boldsymbol{v}}^*_\beta \\ \hat{\boldsymbol{v}}^*_\gamma \end{bmatrix} \tag{16}$$

$$d_1 = 1 - d_2 - d_3 - d_4 \tag{17}$$

where d_1 to d_4 represent the duty cycle of each of the four vectors that modulate the reference vector and the matrix $\boldsymbol{D_n}$ takes six different values depending on the sector according to (15) (see Appendix).

A. Switching Sequence and Power Losses

After the stationary vectors and their dwell times have been obtained, a switching pattern that arrange these vectors during the sampling time T_s has to be defined. The selection of this pattern, also known as the switching sequence, is always a trade-off between the number of commutations, i.e. switching power losses, and the accuracy of tracking a reference signal, i.e. current or voltage ripple. Therefore, the selection between different patterns mostly depends on the application. In this paper a single redundancy switching pattern is defined and implemented. This pattern uses only one of all the available redundant vectors at each sampling time. This reduces the switching frequency of the devices and also distributes the power losses uniformly among the devices. Fig. 7 shows an example of the commutation sequence for the modulation of a reference vector inside a tetrahedron formed by the vectors: $\boldsymbol{v}_4$, $\boldsymbol{v}_{15}$, $\boldsymbol{v}_1$, $\boldsymbol{v}_{10}$. Although vectors $\boldsymbol{v}_1$, $\boldsymbol{v}_4$ and $\boldsymbol{v}_{10}$ posses one redundancy, only the redundancy of the vector $\boldsymbol{v}_4$ has been used.

As shown in Fig. 7, regardless of the path described by the reference vector in Fig. 6, always one commutation takes place at every sampling time. Thereby, considering that *ac* signals are being modulated, the switching frequency per device over a fundamental cycle in a four-leg NPC converter, is given by:

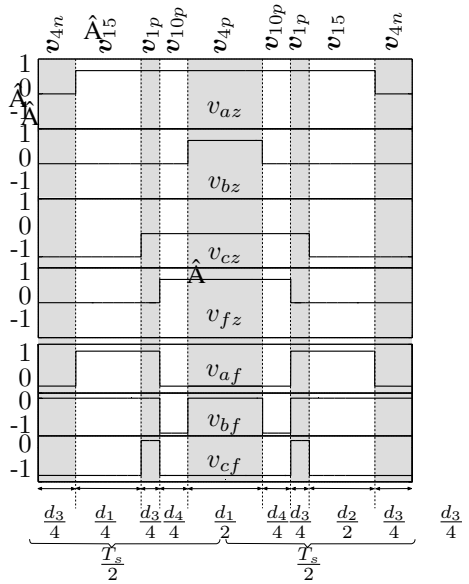

Fig. 7. Switching commutation based on a Single Redundancy switching pattern. The vectors that compose the selected tetrahedron are: $\boldsymbol{v}_4$ ([OONO] or [PPOP]), $\boldsymbol{v}_{15}$ ([PONO]), $\boldsymbol{v}_1$ ([ONNN] or [POOO]), $\boldsymbol{v}_{10}$ ([ONNO] or [POOP]), where P, N and O stands for positive, zero or negative output voltage of each leg of the four-leg NPC converter.

$$\bar{f}_{dev} = \frac{f_s}{2}, \tag{18}$$

where f_s represents the sampling frequency and $\bar{f}_{dev}$ is the average switching frequency of each of the four switching devices of each leg of the converter. Notice that the equivalent switching frequency of the output voltage is still f_s. This is an important advantage compared with a two-level inverter, where the switching frequency of each device is equal to the equivalent frequency of the modulated waveform, i.e. f_s.

IV. Experimental Validation

The experimental rig used to validate the proposed controller in a four-leg NPC is illustrated in Fig. 8 (load is not shown). The control system hardware is composed of a Pentium-System board (3.2GHz Pentium processor, 2Gb RAM host PC, based on the Arch-Linux operating system) and an FPGA board connected via an ISA-bus. This platform runs the algorithm using the Real Time Application Interface (RTAI) for Linux. The FPGA board manages the ADCs, implements the over-voltage and over-current protections, performs the dead time and generates the IGBT switching signals. Optical fibers are used to transmit the IGBT gate signals from the FPGA output buffer to the NPC converter.

A four-leg NPC converter has been designed based on the Microsemi IGBT-APTGL60TL120T3G rated at 60A and 1200V. The nominal power of the experimental prototype is 6kVA. The experimental results presented in this Section utilize step impacts and steady state connection of linear/non-linear unbalanced loads in order to verify the performance of the prototype and its capacity to fulfill the standards of [2].

A. Experimental Results

In order to validate the proposed topology and control design, the aircraft of Fig. 1 is replaced by linear/non-linear,

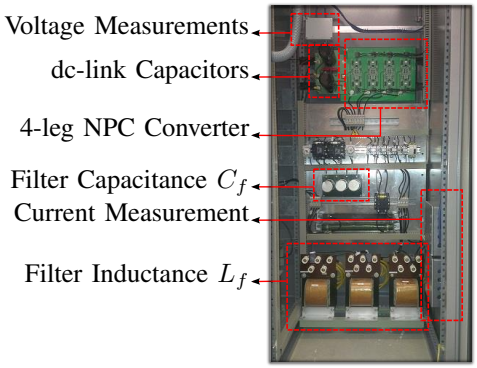

Fig. 8. Experimental rig for a four-leg NPC converter

balanced/unbalanced loads in the experimental rig. The steady-state and transient performance is investigated in the following sections. Table II gives the common parameters used for the experimental results.

TABLE II
GENERAL PARAMETERS OF THE IMPLEMENTED SYSTEMS

Parameter	Value	Parameter	Value
C_1	3300 uF	Z	$10\,\Omega$; $0.8\,mH$
C_2	3300 uF	Z_{a2}	$10\,\Omega$; $0.8\,mH$
V_{dc}	325 V	Z_{b2}	$14\,\Omega$; $0.8\,mH$
C_f	20 uF	Z_{c2}	$18\,\Omega$; $0.8\,mH$
L_f	219 uH	Single/Three-phase Full Wave	$220\,uF$; $57\,\Omega$
f_{sw}	16.8 kHz	Diode Bridge Rectifier	

1) Steady-State Performance: Fig. 9 shows the performance of the proposed system of Fig. 1 under unbalanced operation, using Z_{a2}, Z_{b2} and Z_{c2}. The power consumption of each branch is: 1.21kW, 0.86kW and 0.67kW respectively. As depicted in Fig. 1, the controller compensates the different voltage drops on each phase of the filter and maintains the output voltages at 110V, 400Hz. Note that the neutral current has a reduced harmonic distortion due to cancellation of some of the harmonic components in the line currents. The THDs of each output voltage are 0.87%, 0.92%, 1.10% respectively, which easily meets the maximum of 5% required by the standard [2].

In order to evaluate the performance of the proposed topology and control strategy when feeding non-linear loads, a three-phase and a single-phase full wave diode bridge rectifier, both with a RC load at the dc side, are connected at the output of the GPU (see Table II). Fig. 11 shows the reference voltage generated by the controller, which is then synthesized by the 3D-SVM [24], [25]. Clearly, the reference voltage is far from an ideal sinusoidal shape. However, this is the required waveform to compensate the harmonic voltage drop produced by the distorted current circulating through the filter inductance L_f to subsequently obtain a sinusoidal voltage at the load. To highlight the effectiveness of the high-order harmonics compensation of the proposed method, output voltages and currents of the proposed GPU, considering only compensation of $400Hz$ fundamental waveform, are showed in Fig.12. As result, highly distorted output voltages are obtained, with a THDv of 9.8% on each phase approximately.

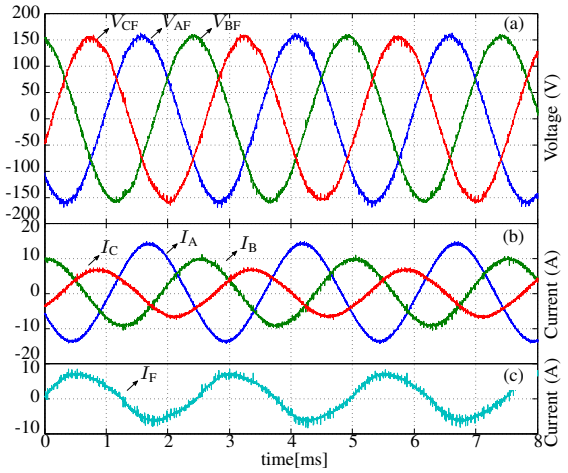

Fig. 9. Performance of the proposed GPU under a 2.8 kW, linear-unbalanced load (Z_{a2}, Z_{b2}, Z_{c2}). Sampling frequency of f_s=16.8kHz. (a) output voltages V_{AF}, V_{BF}, V_{CF}, (b) line currents I_A, I_B, I_C and (c) neutral wire current I_F.

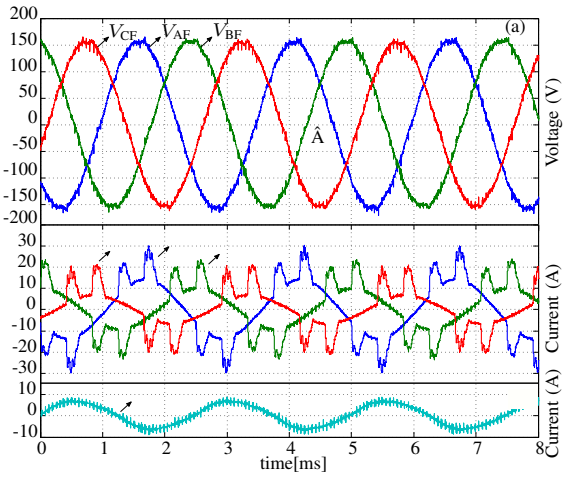

Fig. 10. Performance of the proposed GPU under a 2.8kW linear-unbalanced load (Z_{a2}, Z_{b2}, Z_{c2}) and a 1.27kW three-phase full wave diode bridge rectifier (57Ω and 220uF). Sampling frequency of f_s=16.8kHz.(a) output voltages V_{AF}, V_{BF}, V_{CF}, (b) line currents I_A, I_B, I_C and (c) neutral wire current I_F.

Finally, Fig. 13 shows the performance of the proposed GPU for a test using a 0.42kW single-phase full wave diode bridge rectifier and a 2.8kW linear-unbalanced load (Z_{a2}, Z_{b2}, Z_{c2}). As the single-phase full wave diode bridge rectifier introduces a distorted zero sequence component, the neutral current is not sinusoidal and contains the harmonics generated by the rectifier. This current also contains some even harmonics which are not compensated by the controller. Hence, although the THD is within the required limit for each phase (3.07%, 1.2% and 1.2% respectively), the phase where the single-phase rectifier is connected has the highest harmonic distortion.

2) Transient Performance: Fig. 14 illustrates a transient from unbalanced operation to a full balanced load, while Fig. 15 shows a load impact from nominal balanced load to open circuit (The parameters of the load step are given in Table II). In both cases the controller achieves a good dynamic response, compensating the transient after approximately 1-2 cycles (2.5ms-5ms), easily meeting the transient requirements

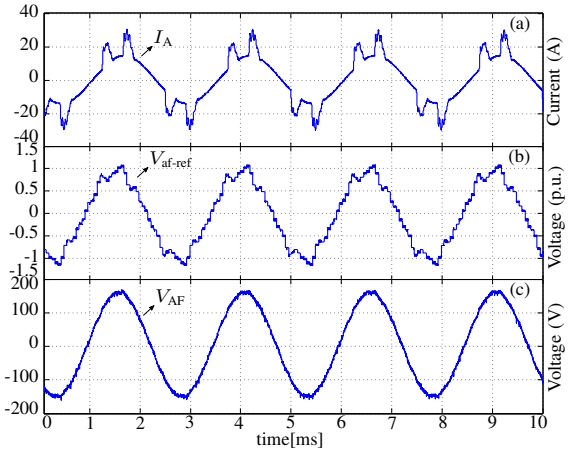

Fig. 11. Performance of the proposed GPU under a 2.8kW linear-unbalanced load (Z_{a2}, Z_{b2}, Z_{c2}) and a 1.27kW three-phase full wave diode bridge rectifier (57Ω and 220 uF). Sampling frequency of f_s=16.8kHz. (a) line current I_A, (b) reference voltage for the converter $V_{af\text{-}ref}$ and (c) GPU output voltage V_{AF}.

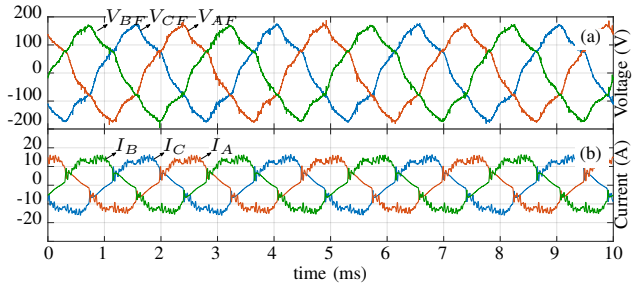

Fig. 12. Performance of the proposed GPU under a 2.5kW linear-balanced load (Z) and a 1.27kW three-phase full wave diode bridge rectifier (57Ω and 220 uF). Compensation of only fundamental $400Hz$ component (f_s=16.8kHz). (a) Output voltages V_{AF}, V_{BF} and V_{CF} and (b) output currents I_A, I_B, I_C. $THD_V \approx 9.8\%$.

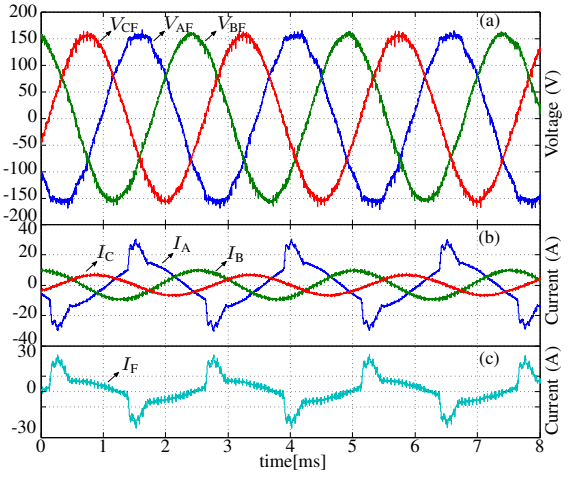

Fig. 13. Performance of the proposed GPU under a 2.8kW linear-unbalanced load (Z_{a2}, Z_{b2}, Z_{c2}) and a 0.42kW three-phase full wave diode bridge rectifier (57Ω and 220uF). Sampling frequency of f_s=16.8kHz. (a) voltages V_{AF}, V_{BF}, V_{CF}, (b) line currents I_A, I_B, I_C and (c) neutral wire current I_F.

in [2]. Fig 16 shows the regulation of the voltages on the dc-link capacitors after a load impact: from no-load condition to the 2.8kW linear-unbalanced load. The voltage deviation is lower than 5V, converging to the reference after around 60 ms. This validates the effectiveness of the voltage balance algorithm used on the 3D-SVM and the appropriate design of the PI controller utilized for balancing the voltage on each capacitor [24], [25].

Fig. 17 presents the transient response for a 1.27kW load-impact connected at the output of a three-phase full wave diode bridge rectifier. Even considering that this is a large load impact, the controller can reject this disturbance after approximately 10 ms (3-4 cycles). As the capacitor is not charged before the load impact, it behaves as a short circuit and the voltage is not controllable for around 1 cycle. Additionally, the upper and lower transient boundaries of the standard are also depicted in Fig. 17a to highlight that the transient response easily meets the required standard [2], which allows an over-voltage of 118V after 87.5 ms.

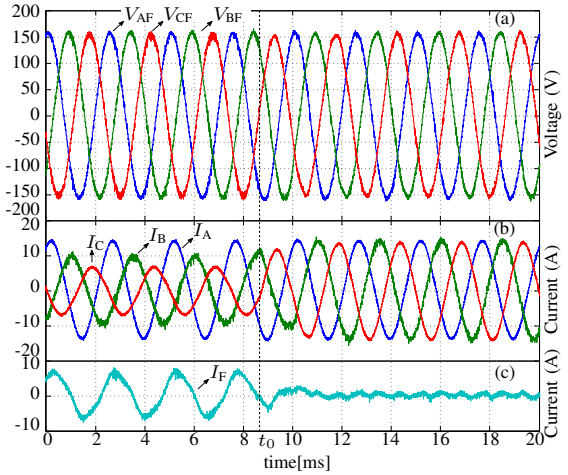

Fig. 14. Transient response of the proposed GPU for a load step: from a 2.8kW unbalanced load to a 3.6kW balanced load. (a) output voltages V_{AF}, V_{BF}, V_{CF}, (b) line currents I_A, I_B, I_C and (c) the neutral wire current I_F.

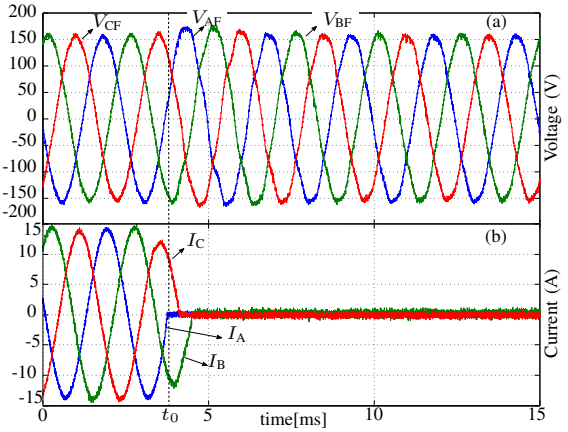

Fig. 15. Transient response of the proposed GPU for a load step: from 3.6kW balanced load to open circuit. (a) output voltages V_{AF}, V_{BF}, V_{CF} and (b) the line currents I_A, I_B, I_C.

V. Conclusion

This paper has proposed a simple methodology to design multiple resonant controllers for high-order harmonics compensation when small ratio between sampling frequency and harmonic compensated frequencies is required. Unlike

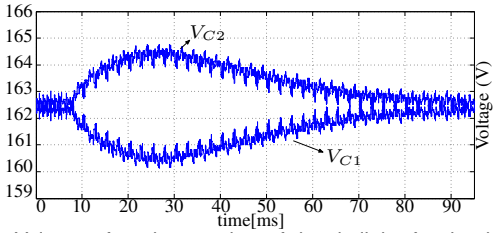

Fig. 16. Voltage of each capacitor of the dc-link after load step: from open circuit to a 2.8kW unbalanced load. The capacitors return to a balanced condition after the transient.

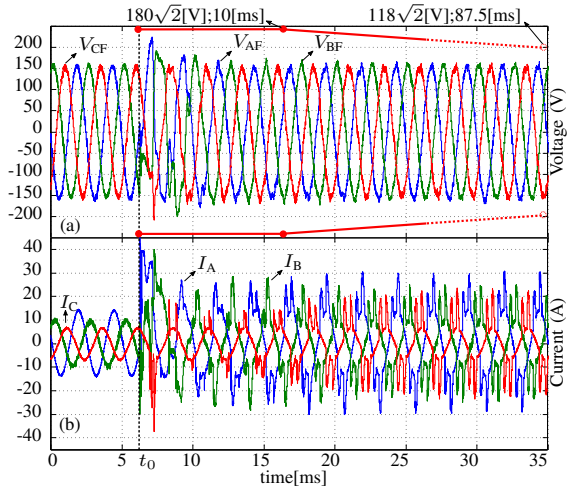

Fig. 17. Transient response of the proposed GPU for a 1.27kW three-phase full wave diode bridge rectifier load impact from a 2.8kW unbalanced load. (a) output voltages V_{AF}, V_{BF}, V_{CF} and (b) the line currents I_A, I_B, I_C.

previous methodologies, the work proposed in this paper does not assume decoupled operation of the resonant controllers, taking in consideration the full dynamic of the plant and controllers. The method is based on Nyquist diagrams and it also allows the design of multiple resonant controllers when a second-order output filter is used at the GPU output. This methodology overcome typical difficulties associated with Bode design methods for high-order controllers with multiple resonant peaks. In addition, it overcome the problem of designing resonant controllers when the resonance frequency is close to the filter resonance frequency.

In order to achieve high-order harmonics compensation at 400Hz fundamental waveform, a 4-leg NPC converter is proposed as solution. Thus, a double equivalent output frequency compared to the switching frequency per device is obtained. This allows the use of smaller power filters, lower switching losses and higher harmonics compensation. A resonant controller designed to regulate a fundamental signal of 400Hz and eliminate the 3rd, 5th, 7th, 9th and 11th harmonics from the load voltage were successfully designed and experimentally validated.

Experimental results have been conducted in a 6kW prototype to validate the proposed methodology in a GPU application. The converter has been tested under unbalanced and non-linear loads performing excellent results maintaining sinusoidal output voltages under transient and steady state operation. Furthermore, it is also demonstrated that dc-link voltage balancing can be also achieved even in the presence of severely unloaded non-linear load.

VI. Appendix

$$\boldsymbol{T}_{abc}^{\alpha\beta\gamma} = \frac{2}{3}\begin{bmatrix} 1 & -1/2 & -1/2 \\ 0 & \sqrt{3}/2 & -\sqrt{3}/2 \\ 1/2 & 1/2 & 1/2 \end{bmatrix} \tag{19}$$

The matrix $\boldsymbol{D}_n$ can be expressed for each interval as $\phi \in \left[\frac{(n-1)\pi}{3}, \frac{n\pi}{3}\right[$; $n \in \{1,2,3,4,5,6\}$:

$$\boldsymbol{D}_1 = \begin{bmatrix} \frac{3}{2} & -\frac{\sqrt{3}}{2} & 0 \\ 0 & \sqrt{3} & 0 \\ -\frac{1}{2} & -\frac{\sqrt{3}}{2} & 1 \end{bmatrix} \quad \boldsymbol{D}_4 = \begin{bmatrix} 0 & -\sqrt{3} & 0 \\ -\frac{3}{2} & \frac{\sqrt{3}}{2} & 0 \\ 1 & 0 & 1 \end{bmatrix}$$

$$\boldsymbol{D}_2 = \begin{bmatrix} -\frac{3}{2} & \frac{\sqrt{3}}{2} & 0 \\ \frac{3}{2} & \frac{\sqrt{3}}{2} & 0 \\ -\frac{1}{2} & -\frac{\sqrt{3}}{2} & 1 \end{bmatrix} \quad \boldsymbol{D}_5 = \begin{bmatrix} -\frac{3}{2} & -\frac{\sqrt{3}}{2} & 0 \\ \frac{3}{2} & -\frac{\sqrt{3}}{2} & 0 \\ -\frac{1}{2} & \frac{\sqrt{3}}{2} & 1 \end{bmatrix}$$

$$\boldsymbol{D}_3 = \begin{bmatrix} 0 & \sqrt{3} & 0 \\ -\frac{3}{2} & -\frac{\sqrt{3}}{2} & 0 \\ 1 & 0 & 1 \end{bmatrix} \quad \boldsymbol{D}_6 = \begin{bmatrix} \frac{3}{2} & \frac{\sqrt{3}}{2} & 0 \\ 0 & -\sqrt{3} & 0 \\ -\frac{1}{2} & \frac{\sqrt{3}}{2} & 1 \end{bmatrix} \tag{20}$$

References

[1] T. Wijekoon, L. Empringham, P. W. Wheeler, J. C. Clare, C. Whitley, and G. Towers, "Aircraft Electrical Landing Gear Actuation Using Dual-output Power Converter with Mutual Power Circuit Components," in *2009 Twenty-Fourth Annual IEEE Applied Power Electronics Conference and Exposition*. IEEE, feb 2009, pp. 1263–1268.

[2] MILITARY STANDARD, "MIL-STD-704F Aircraft Electric Power Characteristics."

[3] SAE, "AIR6139 Ways of Dealing with Power Regeneration onto an Aircraft Electrical Power System Bus."

[4] U. B. Jensen, F. Blaabjerg, and J. K. Pedersen, "A new control method for 400-Hz ground power units for airplanes," *IEEE Transactions on Industry Applications*, vol. 36, no. 1, pp. 180–187, 2000.

[5] Zixin Li, Yaohua Li, Ping Wang, Haibin Zhu, Congwei Liu, and Fanqiang Gao, "Single-Loop Digital Control of High-Power 400-Hz Ground Power Unit for Airplanes," *IEEE Transactions on Industrial Electronics*, vol. 57, no. 2, pp. 532–543, feb 2010.

[6] Muthu, "US5387859 A Stepped waveform VSCF system with engine start capability," 1993.

[7] S. Lopez Arevalo, P. Zanchetta, P. W. Wheeler, A. Trentin, and L. Empringham, "Control and Implementation of a Matrix-Converter-Based AC Ground Power-Supply Unit for Aircraft Servicing," *IEEE Transactions on Industrial Electronics*, vol. 57, no. 6, pp. 2076–2084, jun 2010.

[8] P. Wheeler, A. Trentin, S. Bozhko, and J. Clare, "Regeneration of energy onto an aircraft electrical power system from an electro-mechanical actuator," in *2012 Electrical Systems for Aircraft, Railway and Ship Propulsion*. IEEE, oct 2012, pp. 1–6.

[9] G. Escobar, A. A. Valdez, J. Leyva-Ramos, and P. Mattavelli, "Repetitive-Based Controller for a UPS Inverter to Compensate Unbalance and Harmonic Distortion," *IEEE Transactions on Industrial Electronics*, vol. 54, no. 1, pp. 504–510, feb 2007.

[10] P. Cortes, G. Ortiz, J. I. Yuz, J. Rodriguez, S. Vazquez, and L. G. Franquelo, "Model Predictive Control of an Inverter With Output LC Filter for UPS Applications," *IEEE Transactions on Industrial Electronics*, vol. 56, no. 6, pp. 1875–1883, jun 2009.

[11] W. Rohouma, P. Zanchetta, P. W. Wheeler, and L. Empringham, "A Four-Leg Matrix Converter Ground Power Unit With Repetitive Voltage Control," *IEEE Transactions on Industrial Electronics*, vol. 62, no. 4, pp. 2032–2040, 2015.

[12] R. Cardenas, C. Juri, R. Peña, P. Wheeler, and J. Clare, "The Application of Resonant Controllers to Four-Leg Matrix Converters Feeding Unbalanced or Nonlinear Loads," *IEEE Transactions on Power Electronics*, vol. 27, no. 3, pp. 1120–1129, 2012.

[13] A. G. Yepes, F. D. Freijedo, O. Lopez, and J. Doval-Gandoy, "Analysis and Design of Resonant Current Controllers for Voltage-Source Converters by Means of Nyquist Diagrams and Sensitivity Function," *IEEE Transactions on Industrial Electronics*, vol. 58, no. 11, pp. 5231–5250, nov 2011.

[14] A. G. Yepes, F. D. Freijedo, J. Doval-Gandoy, O. Lopez, J. Malvar, and P. Fernandez-Comesana, "Effects of Discretization Methods on the Performance of Resonant Controllers," *IEEE Transactions on Power Electronics*, vol. 25, no. 7, pp. 1692–1712, jul 2010.
[15] G.C. Goodwin, S.F. Graebe and M. Salgado, *Control System Design*, 1st ed. Prentice Hall PTR Upper Saddle River, NJ, USA, 2000.
[16] C. Lascu, L. Asiminoaei, I. Boldea, and F. Blaabjerg, "High Performance Current Controller for Selective Harmonic Compensation in Active Power Filters," *IEEE Transactions on Power Electronics*, vol. 22, no. 5, pp. 1826–1835, sep 2007.
[17] C. Lascu, L. Asiminoaei, and I. Boldea, "Frequency Response Analysis of Current Controllers for Selective Harmonic Compensation in Active Power Filters," *IEEE Transactions on Industrial Electronics*, vol. 56, no. 2, pp. 337–347, feb 2009.
[18] S. Fukuda and T. Yoda, "A novel current-tracking method for active filters based on a sinusoidal internal model [for PWM invertors]," *IEEE Transactions on Industry Applications*, vol. 37, no. 3, pp. 888–895, 2001.
[19] R. Bojoi, G. Griva, V. Bostan, M. Guerriero, F. Farina, and F. Profumo, "Current Control Strategy for Power Conditioners Using Sinusoidal Signal Integrators in Synchronous Reference Frame," *IEEE Transactions on Power Electronics*, vol. 20, no. 6, pp. 1402–1412, nov 2005.
[20] D. Floricau, G. Gateau, A. Leredde, and R. Teodorescu, "The efficiency of three-level Active NPC converter for different PWM strategies," in *Power Electronics and Applications, EPE '09.*, 2009, pp. 1–9.
[21] F. Blaabjerg, R. Teodorescu, M. Liserre, and A. V. Timbus, "Overview of Control and Grid Synchronization for Distributed Power Generation Systems," *IEEE Transactions on Industrial Electronics*, vol. 53, no. 5, pp. 1398–1409, 2006.
[22] F. Blaabjerg, Z. Chen, and S. B. Kjaer, "Power electronics as efficient interface in dispersed power generation systems," *IEEE Transactions on Power Electronics*, vol. 19, no. 5, pp. 1184–1194, sep 2004.
[23] D. Zmood and D. Holmes, "Stationary frame current regulation of PWM inverters with zero steady-state error," *IEEE Transactions on Power Electronics*, vol. 18, no. 3, pp. 814–822, may 2003.
[24] F. Rojas, R. Cárdenas, R. Kennel, J. C. Clare, and M. Díaz, "A Simplified Space-Vector Modulation Algorithm for Four-Leg NPC Converters," *IEEE Transactions on Power Electronics*, vol. 32, no. 11, pp. 8371–8380, 2017.
[25] F. Rojas, R. Kennel, R. Cardenas, R. Repenning, J. C. Clare, and M. Diaz, "A New Space-Vector-Modulation Algorithm for a Three-Level Four-Leg NPC Inverter," *IEEE Transactions on Energy Conversion*, vol. 32, no. 1, pp. 23–35, mar 2017.

Félix Rojas (M'12) was born in Santiago, Chile. He received the B.Eng. and M.Sc. degrees in electrical engineering with highest honours in 2009, from the Universidad de Santiago de Chile. In 2015, he obtained his doctoral degree from the Technical University of Munich, Germany. He is currently Assistant Professor at the Universidad de Santiago de Chile and he is also an Research Associate of the Solar Energy Research Center (SERC Chile). His research interests are in control of power electronics converters for solar and wind energy conversion, power networks conditioning, high power electric vehicles chargers and variable speed drives.

Roberto Cárdenas (S'95-M'97-SM'07) was born in Punta Arenas Chile. He received his B.S. degree from the University of Magallanes, Chile, in 1988 and his Msc. and Ph.D degrees from the University of Nottingham in 1992 and 1996 respectively. From 1989-1991 and 1996-2008 he was a lecturer in the University of Magallanes Chile. From 1991 to 1996 he was with the Power Electronics Machines and Control Group (PEMC group), University of Nottingham, United Kingdom. From 2009-2011 he was with the Electrical Engineering Department, University of Santiago. He is currently a professor of power electronics and drives in the Electrical Engineering Department, University of Chile, Chile. His main interests are in control of electrical machines, variable speed drives and renewable energy systems.

Jon C. Clare (M'90-SM'04) was born in Bristol, U.K., in 1957. He received the B.Sc. and Ph.D. degrees in electrical engineering from the University of Bristol, Bristol. From 1984 to 1990, he was a Research Assistant and Lecturer with the University of Bristol, where he was involved in teaching and research on power electronic systems. Since 1990, he has been with the Power Electronics, Machines and Control Group, The University of Nottingham, Nottingham, U.K., where he is currently a Professor of power electronics. His research interests include power-electronic converters and modulation strategies, variable-speed-drive systems, and electromagnetic compatibility.

Matías Díaz (S'15) was born in Santiago, Chile. In 2011, he received the B.Sc. and M.Sc. degrees in electrical engineering from the University of Santiago of Chile, Chile. In 2017, he obtained a dual Ph.D. degree at the University of Nottingham, United Kingdom, and at the University of Chile, Chile. Dr. Matías Díaz is an Assistant Professor at the University of Santiago of Chile. His main research interests include the control of wind energy conversion systems and multilevel converters.

Javier Pereda (S'09-M'14) received a B.Sc. (Eng) with highest honors from Pontificia Universidad Católica de Chile, Santiago, in 2009, and a M.Sc and Ph.D from the same university in 2013. All degrees were in electrical engineering. He is currently an Assistant Professor of the Department of Electrical Engineering at Pontificia Universidad Católica de Chile since 2013. From 2014 to 2016, he was Research Associate of the Control and Power Group in the Electrical and Electronic Engineering Department at Imperial College London. He is an Research Associate of the Solar Energy Research Center (SERC Chile) and the UC Energy Research Center. He is the principal investigator of the Electric Vehicle Laboratory and the Power and Energy Conversion Laboratory (PEClab) at Pontificia Universidad Católica de Chile. His research interests are power electronics and control applied to electric vehicles, AC and DC electric networks, microgrids, renewable energy, industrial applications and motor drives.

Ralph Kennel (M'90-SM'96) received the diploma degree in 1979 and the Dr.-Ing. (Ph.D.) degree in 1984 from the University of Kaiserslautern, Kaiser-slautern, Germany. From 1983 to 1999, he worked on several positions with Robert BOSCH GmbH, Stuttgart, Germany. Until 1997, he was responsible for the development of servo drives. From 1994 to 1999, he was appointed as a Visiting Professor at the University of Newcastleupon-Tyne, England, U.K. From 1999 to 2008, he was a Professor for electrical machines and drives at Wuppertal University, Wuppertal, Germany. Since 2008, he has been a Professor for electrical drive systems and power electronics at Technische Universtat Muenchen, Germany. His main interests today are: sensorless control of ac drives, predictive control of power electronics, and hardware-in-the-Loop systems.